The potential impacts of pollution on a nondrizzling stratus deck: Does aerosol number matter more than type?

M. Andrejczuk,[1] J. M. Reisner,[1] B. Henson,[1] M. K. Dubey[1] and C. A. Jeffery[1]

[1]   In this paper results from a cloud-resolving model that can efficiently examine the impact of aerosol on nondrizzling stratus clouds will be shown. Because the model tracks aerosol and cloud droplets in a Lagrangian framework, it does not suffer from numerical errors associated with advection, and unlike most Eulerian approaches, the method can track cloud boundaries as they move across a grid cell. After illustrating the capability of the model to reproduce various observed cloud statistics such as the cloud water mixing ratio and the mean cloud droplet radius from the DYCOMS-II field program, the ability of the model to assess the impact of changes in aerosol number and composition on a stratus deck will be highlighted. Specifically, by using activation curves appropriate for soluble, insoluble, or a mixture of both types of aerosol and for certain extreme aerosol regimes, i.e., a majority of the aerosol are hydrophobic carbon aerosol, limiting situations were examined to bound their impact on clouds. However, though these situations may be somewhat extreme, they could occasionally occur in the atmosphere, e.g., an oceanic stratus field downwind of a large ship or an urban area. Not unexpectedly, results from these simulations support previous ship track observations that for increasing aerosol numbers, cloud droplet number concentrations increase, whereas cloud droplet radii decrease. However, these simulations also suggest that the correlation between cloud droplet number concentration and aerosol number concentration may be not only a function of aerosol number concentration but also aerosol types and/or cloud dynamics.

1.   Introduction

[2]   The Earth's atmosphere typically contains a mixture of different types of aerosols that are produced by natural or anthropogenic processes. Not unexpectedly, aerosol play an important role in weather and climate through direct or indirect mechanisms. For example, a direct mechanism involves the ability of aerosol to influence the Earth's energy budget by either reflecting and/or absorbing radiation [*Twomey*, 1974; *Bergstrom et al.*, 2002], whereas, by serving as cloud condensation nuclei (CCN), an indirect process is the impact of aerosol on cloud droplet concentration and also the mean cloud droplet radius, r_{mean}, and subsequent overall radiation budget.

[3]   Because of the abundance of stratus clouds over vast stretches of the Earth's atmosphere, any changes in their mean properties via the indirect effect can have a rather large impact on the Earth's climate [*Durkee et al.*, 2000]. For instance, if anthropogenic processes lead to the formation of high quantities of aerosol that advect into a stratus deck, then key cloud properties, such as r_{mean} and the total cloud droplet number concentration, Nc_t, could change

substantially leading to rather significant changes in the overall radiation budget. To help isolate the impact of anthropogenic aerosol on cloud properties, previous researchers have investigated ship tracks and have noted, for example, during the MAST field program [*Durkee et al.*, 2000; *Ferek et al.*, 2000; *Ackerman et al.*, 2000; *Hudson et al.*, 2000] for increasing ship emissions that Nc_t goes up while r_{mean} goes down. However, this relationship is by no means unique to ship trails in *Yum and Hudson* [2002] showing that this relationship also holds in both continental and marine stratus clouds.

[4]   To further build upon these previous findings and to also highlight the impact on cloud dynamics of a changing aerosol field, cloud-resolving simulations of a nondrizzling nocturnal stratus field similar to that observed during flight one DYCOMS-II [*Stevens et al.*, 2005, hereafter RF01] will be conducted. Because the aerosol employed in the present simulations is well mixed throughout the computational domain, these simulations are not intended to reproduce ship tracks, rather they are intended to at least partially understand the impact of pollution via anthropogenic aerosol on a stratus deck. Specifically, this study will examine the possible impact of black carbon (BC) aerosol on stratus clouds by using activation curves appropriate either for BC aerosol having different "wetting" abilities [*Rudzinski and Everett*, 1992], i.e., the ability of water to condense onto this aerosol, which is typically a function of aerosol age and the

---

[1]Los Alamos National Laboratory, Los Alamos, New Mexico, USA.

combustion process, or an activation curve [*Pruppacher and Klett*, 1978] appropriate for aerosol containing a certain percentage of insoluble (carbon-BC) and soluble (ammonium sulfate-AS) parts. Further, the additional aerosol will be added at a size range for which type plays a significant role during activation with the mean radius of this additional aerosol being in rough agreement with the observed spectra of carbon aerosol obtained under biomass burning in Brazil [*Martins et al.*, 1998].

[5] While a recent observational study [*Dusek et al.*, 2006] suggests that number is more important than type in determining key cloud quantities, in contrast, studies by *Twohy et al.* [2005] (see Figure 4) and *Hudson* [2007] show that these quantities do depend on aerosol type. Hence given the conflicting findings and the difficulties in isolating from the observations what is producing the differences, a simulation based approach will be conducted in this paper in which extreme differences in the aerosol makeup, e.g., all BC aerosol are either hydrophobic or hydrophilic, are specified, hence enabling the biggest impact of type on key bulk cloud quantities such as the cloud water mixing ratio, q_c, and possibly dynamics, to be quantified. Further, when examining the potential impact of aerosol type on cloud dynamics and microphysics, simulations will be conducted in which aerosol concentration and size are held constant, with only type being varied. Additionally, given that aerosol type may be more difficult to obtain than number [*Durkee et al.*, 2000], the present model could, in the future, when coupled with some type of minimization procedure, be used in a forensic sense to roughly infer the chemical makeup of an observed aerosol distribution.

[6] For this study both aerosol and cloud droplets will be modeled using a Lagrangian particle approach, whereas the gas phase will be simulated using the traditional continuous form of the Navier-Stokes equation set utilizing a large-eddy simulation (LES) approach [*Reisner et al.*, 2003] for representing unresolved processes. In this paper the entire model will be referred to as a Lagrangian Cloud Model (LCM). Note, unlike diagnostic particle approaches for which the particles are only used to calculate quantities such as in-cloud residence time [*Stevens et al.*, 1996a; *Feingold et al.*, 1996; *Kogan*, 2006] within the LCM framework, particles, both aerosol and cloud droplets, directly impact the momentum, energy, and mass of the gas phase. In addition, even though the simulations are for a nondrizzling stratus cloud, particles still have a fall velocity relative to the air, via the gravitational acceleration term found in the vertical equation of motion for the particles, with this fall velocity being an important aspect in maintaining the thickness of the stratus cloud.

[7] Due to the ability of the LCM framework to accurately simulate processes responsible for producing entrainment events, the sub-grid gravitational settling of particles and any cooling associated with water evaporating off these downward moving particles, the LCM, unlike most Eulerian approaches employing modest grid resolutions, has the potential to accurately capture entrainment events routinely found within stratus clouds. Further, entrainment will be defined, within the context of the LCM framework applied to stratus clouds, to be the relatively rapid downward movement of particles from cloud top to bottom with turbulent motions playing little if any role in this process,

i.e., particle motions are primarily produced by the resolved velocity fields of the dynamical model. Moreover, the current coupled approach enables particles to be impacted by a highly nonlinear-in-time supersaturation field–and vice versa—with this two-way interaction being difficult to replicate within a simple parcel modeling framework typically used to understand the impact of aerosol on microphysical quantities [*Nenes et al.*, 2001; *Nenes and Seinfeld*, 2003; *Fountoukis and Nenes*, 2005; *Barahona and Nenes*, 2007].

[8] Though the LCM framework is typically not utilized in atmospheric science, this approach has been successfully used in other fields [*DaSilva et al.*, 2006; *Iacono and Reynolds*, 2005; *Matida et al.*, 2004; *Schwere et al.*, 2002]. Indeed, for the current application of condensational growth from aerosol and then the potential evaporation of cloud droplets back into aerosol, the LCM framework is possibly the only framework in which these calculations could have been conducted using a reasonable amount of computational resources. Further, comparisons within a simpler parcel model setting between the LCM framework and the required two-dimensional bin approach, e.g., the bin model spans both droplet and aerosol space [*Kogan*, 1991], reveal that even in this setting the computational cost of the bin approach to produce the same error as from the LCM framework is excessive.

[9] Because of the expense of the bin model and the rather surprising lack of usage of the LCM framework within the atmospheric science community, only a few relatively idealized studies have been made utilizing the complete condensational growth equation model [*Clark*, 1973; *Flossmann*, 1998]. Thus, the LCM simulations for RF01 will hopefully serve to build upon these previous numerical studies and illustrate to the community a new numerical tool to examine the impact of aerosol on a realistic cloud field. Fortunately, because the observed nocturnal stratus field did not contain appreciable amounts of drizzle, collision-coalescence between droplets as well as short-wave radiational effects could be neglected during the simulations. Likewise, since a number of simulations in this study will involve an increasing number of hydrophilic aerosol being added to a background environment composed of AS aerosol, this additional aerosol should significantly reduce the occurrence of drizzle within a stratus cloud [*Albrecht*, 1989], thus further justifying our neglect of the collision-coalescence process. Additionally, changes in aerosol due to chemistry and/or coalescence were neglected with the simulations also being two-dimensional to help minimize the computational burden.

[10] Because the observed stratus field from RF01 did not produce drizzle, a relatively sharp bottom edge was associated with the stratus cloud. As noted in several papers [*Grabowski and Smolarkiewicz*, 1990; *Stevens et al.*, 1996b; *Margolin et al.*, 1997; *Kao et al.*, 2000; *Jeffery and Reisner*, 2006], excessive evaporation near cloud edges associated with the inability of numerical schemes to resolve sharp cloud boundaries can produce rather large numerical errors occasionally leading to the complete disappearance of a cloud deck. In fact, *Stevens et al.* [2005, Figure 3] illustrates that for a majority of the Eulerian cloud-resolving simulations the cloud bottom edge continues to rise during the simulations, indicative of numerical errors associated with

inability of the models to resolve this boundary. Because the current approach resolves a cloud edge with Lagrangian particles, numerical errors are potentially much smaller than those produced by Eulerian models with, in fact, LCM simulations of RF01 revealing little rise in the cloud bottom edge.

[11] Two key topics will be discussed in this paper. The first will be to demonstrate the ability of the LCM framework to reasonably reproduce some of the observational data obtained during RF01, whereas the second is the illustration of the impact of aerosol type on key cloud properties within stratus clouds. To assist in illustrating the topics the remainder of the paper is organized as follows: in the next section both the analytical equations and the numerical formulation of the LCM framework will be discussed; in the third section results from the model for various types and numbers of aerosol will be shown along with comparisons against field data; and the last section offers a few concluding remarks and future directions.

2. LCM Framework

[12] The LCM framework is composed of two parts with the first part the hydrodynamical model and the second the Lagrangian particle model. The hydrodynamical model closely follows the model described in *Reisner et al.* [2005] with additional terms being added to enable the exchange of momentum, energy, and mass between the gas and the particles.

2.1. Hydrodynamical Model

[13] The hydrodynamical model is based upon the Navier-Stokes equation set formulated in a generalized coordinate frame in three dimensions; however, for ease of presentation the equation set will be represented in two-dimensional Cartesian space. The momentum equations in this framework are expressed as follows

$$\frac{\partial(u\rho)}{\partial t} + \frac{\partial(uu\rho)}{\partial x} + \frac{\partial(wu\rho)}{\partial z} = -\frac{\partial p'}{\partial x} + \Phi_{m,x}$$
$$+ \frac{\partial(\kappa\rho\tau^{11})}{\partial x} + \frac{\partial(\kappa\rho\tau^{13})}{\partial z}, \qquad (1)$$

$$\frac{\partial(w\rho)}{\partial t} + \frac{\partial(uw\rho)}{\partial x} + \frac{\partial(ww\rho)}{\partial z} = -\frac{\partial p'}{\partial z} - \rho'g + \Phi_{m,z}$$
$$+ \frac{\partial(\kappa\rho\tau^{31})}{\partial x} + \frac{\partial(\kappa\rho\tau^{33})}{\partial z}, \qquad (2)$$

where u is the Cartesian gas velocity in the horizontal, x, direction; w is the Cartesian gas velocity in the vertical, z, direction; ρ is the total density of the air, $\rho = \rho_d + \rho_v$ with ρ_d the dry air density and ρ_v the density of water vapor; g is the acceleration due to gravity; $p' = p - p_e$ is the pressure perturbation with p the pressure of the gas and $p_e = p_e(z)$ the environmental pressure; $\rho' = \rho - \rho_e$ is the density perturbation where $\rho_e = \rho_e(z)$ is the environmental density; and $\tau^{i'j'} = \frac{\partial u^{i'}}{\partial x^{j'}} + \frac{\partial u^{j'}}{\partial x^{i'}} - \frac{2}{3}\delta^{i'j'}\frac{\partial u^{s'}}{\partial x^{s'}}$ is the strain-rate tensor with the indices, i', j', and s' being from 1 to 2. $\Phi_{m,x}$ and $\Phi_{m,z}$ are momentum exchange terms between the gas and the particles, defined in equations (16) and (17).

[14] The energy equation is expressed as

$$\frac{\partial(\theta\rho)}{\partial t} + \frac{\partial(u\theta\rho)}{\partial x} + \frac{\partial(w\theta\rho)}{\partial z} = \frac{\theta\rho L}{TC_p}f_{cond} + f_{surface-energy} + f_{rad}$$
$$+ \frac{\partial F_{\theta x}}{\partial x} + \frac{\partial F_{\theta z}}{\partial z}, \qquad (3)$$

where θ is the potential temperature, $\theta = T\left(\frac{p_o}{p}\right)^{\frac{R_d}{C_p}}$, with T the temperature of the gas, f_{cond} represents the condensational source term produced by the Lagrangian particle model; f_{rad} is a simple parameterization for cloud-top long-wave induced cooling used in the simulations shown by *Stevens et al.* [2005]; and the diffusional flux of potential temperature being defined, e.g., in the x-direction as $F_{\theta x} = \theta\kappa\frac{\partial\theta}{\partial x}$ with κ being the coefficient of diffusion with constants such as C_p being defined in Table 1. The term,

$$f_{surface-energy} = \kappa\rho\frac{\partial\theta}{\partial z}, \qquad (4)$$

represents a flux of internal energy from the ocean's surface. Note, in the simulations, horizontal and vertical motions are produced by a nonlinear combination of the energy flux from the ocean's surface, latent heat release, gravity, long-wave radiation, and subsidence with the balance between these forcings responsible for the long-term maintenance of the stratus cloud. Since volume fractions for both aerosol and cloud droplets are extremely small, $\approx 10^{-6}$, forcing terms associated with particles occupying a volume of space, e.g., equation 12 in *Gu et al.* [2006], have been neglected in both the momentum and energy equations for both the gas and particle phases with the additional assumption being made that particles are always at the same temperature as the gas.

[15] The conservation equations for water vapor density, $\rho_v = q_v\rho$ with q_v the water vapor mixing ratio, and ρ are expressed as

$$\frac{\partial(q_v\rho)}{\partial t} + \frac{\partial(uq_v\rho)}{\partial x} + \frac{\partial(wq_v\rho)}{\partial z} = -f_{cond} + f_{surface-gas}$$
$$+ \frac{\partial F_{q_v x}}{\partial x} + \frac{\partial F_{q_v z}}{\partial z}, \qquad (5)$$

$$\frac{\partial\rho}{\partial t} + \frac{\partial(u\rho)}{\partial x} + \frac{\partial(w\rho)}{\partial z} = -f_{cond} + f_{surface-gas}. \qquad (6)$$

The term, $f_{surface-gas}$, represents the flux of q_v from the ocean surface and is expressed in a form similar to equation (4).

[16] Assuming an ideal gas, the equation of state can be expressed as

$$p = C_o(\rho\theta)^\Gamma, \qquad (7)$$

where $C_o = R_d^\Gamma/p_o^{\frac{R_d}{C_v}}$ with $\Gamma = \frac{C_p}{C_v}$.

Table 1. Values of Constants Used in the Physical Model

Constant	Description of Constant	Value	Units
p_o	base state pressure	10^5	Pa
C_p	specific heat of air at constant pressure	1004	J K^{-1} kg^{-1}
C_v	specific heat of air at constant volume	717	J K^{-1} kg^{-1}
R	universal gas constant	8.314	J K^{-1} mol^{-1}
R_d	gas constant of dry air	287	J K^{-1} kg^{-1}
R_v	gas constant of moist air	467	J K^{-1} kg^{-1}
L	latent heat	2.5×10^6	J kg^{-1}
L_s	turbulent length scale	40.0	m
g	gravity	9.8	m s^{-2}
μ	dynamic viscosity of the gas	1.78×10^{-5}	kg m^{-1}s^{-1}
ρ_w	density of water	1000	kg m^{-3}
M_w	molecular weight of water	18.016×10^{-3}	kg mol^{-1}
M_s	molecular weight of solute, e.g., ammonium sulfate	132.16×10^{-3}	kg mol^{-1}
σ_w	surface tension of water	0.0761	J m^{-2}
d_w	thickness of a unit layer of water	4.59×10^{-10}	m
ρ_{AS}	density of soluble aerosol	1.769×10^3	kg m^{-3}
ρ_{BC}	density of insoluble aerosol	2.267×10^3	kg m^{-3}

[17] The diffusion coefficient found in equations (1), (2), (3), and (5) is determined from a turbulent kinetic energy (TKE) model [*Mellor and Yamada*, 1974] for unresolved processes with the TKE equation being expressed as

$$\frac{\partial (TKE\rho)}{\partial t} + \frac{\partial (uTKE\rho)}{\partial x} + \frac{\partial (wTKE\rho)}{\partial z}$$
$$= \kappa\rho\tau^{i'j'}\frac{\partial u^{i'}}{\partial x^{j'}} + \frac{g\kappa}{\rho}\frac{\partial \rho}{\partial z} - \frac{TKE^2}{L_s} + \frac{\partial F_{TKEx}}{\partial x} + \frac{\partial F_{TKEz}}{\partial z}, \quad (8)$$

with the first term on the right hand side being the shear generation of turbulence, the second term the buoyancy generation of turbulence, the third term the dissipation of turbulence, and the last two terms the diffusion of turbulence where $\kappa = 0.09 L_s\sqrt{TKE}$ with L_s the turbulence length scale taken to be the horizontal grid resolution. For all simulations the amount of viscosity being added by the turbulence model to the gas phase was extremely small with no viscosity being present in the particle simulations. Future work is needed to quantify the role that turbulence plays in both phases; however, given that the model appears to be able to reasonably reproduce observed quantities, the impact of including turbulent fluctuations in the particle model on mean fields such as q_c is probably small with a few sensitivity simulations tentatively supporting this hypothesis.

2.2. Lagrangian Particle Model

[18] The Lagrangian particle model is composed of equations for particle location, velocity, and cloud droplet radius with these equations being expressed as

$$\frac{dx_i}{dt} = v_i \quad (9)$$

$$\frac{dv_i}{dt} = \frac{1}{\tau_p}(v_i^* - v_i) + g\delta_{i,2} \quad (10)$$

$$\frac{dr}{dt} = \frac{G}{r}(S^* - S_{eq}) \quad (11)$$

where x_i is the particle location in space (i = 1, 2); v_i is the particle velocity; v^*_i is the gas velocity at the particle

location, and $\tau_p = \frac{2\rho_p r^2}{9\mu}$ [*Crowe et al.*, 1998] is the velocity relaxation time with r and ρ_p being the radius or the density of either an aerosol particle or a cloud droplet.

[19] In equation (11), S^* is the supersaturation at a particle location and

$$G = \left[\frac{\rho_w R_v T}{e_s D} + \frac{L\rho_w}{kT}\left(\frac{L}{TR_v} - 1\right)\right]^{-1}, \quad (12)$$

where e_s is the saturation vapor pressure, $k = 1.5 \times 10^{-11} T^3 - 4.8 \times 10^{-08} T^2 + 1.0 \times 10^{-04} T - 3.9 \times 10^{-04}$ is the thermal conductivity of air, and $D = 0.015T - 1.93$ is the diffusivity of water vapor.

[20] To solve equation (11) the equilibrium supersaturation, S_{eq}, over the aerosol surface must be calculated using an activation model. In this paper three activation models were utilized with the first model [*Pruppacher and Klett*, 1978], suitable for a soluble aerosol particle being expressed as

$$S_{eq}^s = \exp\left(\frac{2\sigma_w}{R_v T\rho_w r} - \frac{\nu\phi_s m_s M_w/M_s}{4/3\pi r^3 \rho_s'' - m_s}\right), \quad (13)$$

the second model [*Rudzinski and Everett*, 1992; *Henson*, 2007], suitable for an insoluble aerosol particle is expressed as

$$S_{eq}^i = \exp\left(\frac{2\sigma_w}{R_v T\rho_w r}\right)\left[\frac{c - \theta c + 2\theta - \sqrt{c^2(\theta-1)^2 + 4\theta c}}{2\theta(1-c)}\right], \quad (14)$$

and the third model [*Pruppacher and Klett*, 1978], for a mixture of soluble and insoluble aerosol expressed as

$$S_{eq}^m = \exp\left[\frac{2\sigma_w}{R_v T\rho_w r} - \frac{\nu\phi_s \epsilon_m M_w \rho_N r_N^3}{M_s \rho_w (r^3 - r_N^3)}\right], \quad (15)$$

where m_s is the mass of a particular soluble aerosol, ρ_s'' is the density of a mixed particle, $\theta = \frac{r - r_a}{d_w}$ is the number of water layers on insoluble aerosol with radius r_a, ν, the van't Hoff factor, is the number of ions the solute dissociates into in solution, ϕ_s is the molar osmotic coefficient of soluble

substance, $\nu\phi_s = 2$ in equation (13) and 1 in equation (15), and ϵ_m is the mass fraction of soluble aerosol. In equation (14) $c = \exp(-\frac{\Delta G}{RT})$ is the Boltzman term for the two absorption energies in the system with ΔG being the difference between the free energy for a water molecule on the solid surface and the free energy of adsorption onto the water multilayer [*Henson and Robinson*, 2004]. A constant ΔG was used in the simulations (-5.2 kJ/mole, hydrophilic and 33.6 kJ/mole, hydrophobic case) with values coming from [*Henson*, 2007]. In the atmosphere ΔG will change in time as the carbon aerosol ages and mixes with highly soluble substances such as ammonium sulfate, but, once again, the simulations to be presented are intended to represent certain limiting situations that in all actuality may never be present in the atmosphere.

[21] Given a Lagrangian particle, *id*, within a given grid volume, ΔV, containing a prescribed number, M_{id}, of aerosol having the same physical and chemical properties the integrated forcings on the gas for the given volume can be expressed as follows

$$\Phi_{m,x} = \sum_{id} m_{id} \frac{M_{id}}{\Delta V} \frac{(u^* - u_{id})}{\tau_{p,id}} \qquad (16)$$

$$\Phi_{m,z} = \sum_{id} m_{id} \frac{M_{id}}{\Delta V} \frac{(w^* - w_{id})}{\tau_{p,id}} \qquad (17)$$

$$f_{cond} = \sum_{id} \frac{M_{id}}{\Delta V} \frac{dm_{id}}{dt} \qquad (18)$$

where m_{id} is the mass of an aerosol particle, and $\tau_{p,id}$ is the velocity relaxation time for a particle.

2.3. Numerical Approach

[22] For efficiency, a two-step time-split solution procedure is employed to numerically solve the LCM framework with the first part of this approach involving the use of a semi-implicit algorithm to solve the hydrodynamical model, with both the semi-implicit procedure and the discretization of the model being described by *Reisner et al.* [2005]. Note that during this step forcing terms from the particle model are taken from the old time level. For the next step, information from the hydrodynamical model is first linearly interpolated to the particle locations with equation (11) being next solved using a variable time-stepping Rosenbrock solution procedure [*Press et al.*, 1992]. Upon solving for the growth of cloud droplets, equations (9) and (10) are updated using a backward Euler time-stepping approach.

3. Model Setup and Validation

3.1. Model Setup

[23] As discussed in the introduction, one of the primary goals of this paper is to bracket the impact of a polluted atmosphere on key cloud quantities for a non-drizzling stratus field. To accomplish this goal numerous sensitivity simulations will be conducted in which the number, type,

and activation model for aerosol are changed. To ensure that these various simulations have some relationship to reality they will be compared against a reference simulation that was designed to reproduce observational data from RF01. Additionally, as mentioned in the introduction, the primary component of *Stevens et al.* [2005] was not the observations from RF01, but the comparisons of numerous Eulerian cloud-resolving models against the observational data. As such, the initial and boundary conditions for the reference simulation roughly followed what other models used by *Stevens et al.* [2005, see figures in section 2–a.1], except the current simulations are two-dimensional with the model domain spanning 3200 m in the horizontal and 1280 m in the vertical. This domain was resolved by 80 horizontal grid points with a constant resolution of 40 m and 115 vertical grid points with a variable resolution produced by the following relationship

$$\Delta z = 5 + 20 \sin^2\left(\frac{2\pi z}{845}\right), \qquad (19)$$

that enabled the highest vertical resolution of 5 m (units of z in equation (19) are in meters) to be present both near the ocean's surface and the inversion top. The model employed cyclic boundary conditions, i.e., material that laterally leaves the domain must come back into the domain, for all variables in the horizontal direction with bottom or top boundary conditions for all variables coming from turbulent fluxes associated with a given variable. Also, for the horizontal velocity field, no slip boundary conditions were specified at the bottom of the model, whereas at the model top free slip conditions were imposed.

3.2. Initial Aerosol Distribution

[24] The Lagrangian particle model requires that the aerosol distribution be specified over the entire computational domain. For all simulations a background of ammonium sulfate aerosol using a two modal lognormal distribution was utilized and is expressed as

$$n(r_a) = \sum_{i=1,2} \frac{N_i}{\sqrt{2\pi} r_a \ln \sigma_i} \exp\left[-\frac{\ln^2(r_a/r_{g,i})}{2 \ln^2 \sigma_i}\right] \qquad (20)$$

where $r_{g,i}$ is the geometric mean aerosol radius for mode i, σ_i is the geometric standard deviation for mode i, and N_i is the number of aerosol particles for mode i (see Table 2) with $r_{g,i}$ and σ_i taken from an intercomparison study for flight two (RF02, [http://sky.arc.nasa.gov:6996/ack/gcss9/overview.html]) of DYCOMS-II. While keeping mean radius and geometric standard deviation the same as in RF02, the number of aerosol in the second mode has been increased from the 65 cm^{-3} observed during RF02 to 130 cm^{-3} to better approximate the observed relation between aerosol concentration and cloud droplet number concentration for RF01 (*Twohy et al.*, 2005, Figure 1).

[25] This base aerosol distribution is for a relatively clean environment and also roughly agrees with what is shown in *Twohy et al.* [2005, Figure 2 (left)]. To reasonably resolve this aerosol distribution, 1.8 million evenly distributed particles were used which, in the smallest grid cell, is

Table 2. Parameters of the Various Aerosol Distributions with Units of N_i [cm^{-3}], and $r_{g,i}$ [μm][a]

Distribution Type	N_1	$r_{g,1}$	$\sigma_{g,1}$	N_2	$r_{g,2}$	$\sigma_{g,2}$	N_3	$r_{g,3}$	$\sigma_{g,3}$
1	125.0	0.011	1.2	130.0	0.06	1.7			
2							130.0	0.06	1.7
3							260.0	0.06	1.7
4							520.0	0.06	1.7
5							1040.0	0.06	1.7

[a]Note, the reference simulation employs distribution type one and ammonium sulfate aerosol.

roughly 93 particles. After allocating a certain number of particles to each grid cell, a Gaussian random number generator was next used in assigning a radius to each particle between a range of 1×10^{-10} m to 1×10^{-6} m.

[26] Though the initial aerosol distribution was obtained from under the drizzling stratus cloud observed during RF02 and hence does not represent the aerosol distribution that was present during RF01, the impact of these differences on the outcome of the sensitivity simulations should be relatively small. For example, as more hydrophilic aerosol are added near the mean radius of the second mode, the mean cloud droplet radius averaged over the entire computational domain will continue to decrease with the rate of decrease being only weakly related to small changes in the initial location and shape of the second mode. Hence, the current results primarily depend on the characteristics of the additional aerosol and only weakly on the initial base aerosol distribution with even hydrophobic carbon aerosol being able to activate if a large enough initial radius were to

be specified for the additional aerosol, i.e., type matters more than size for only a limited size range. Likewise, if the intent of this paper was to reproduce cloud properties observed during RF01 and not departures from a state that roughly represents the actual conditions, considerable care would be taken to ensure that not only aerosol number but also type as a function of radius agrees with the observed conditions.

[27] The sensitivity simulations have been broken up into 6 groups with each group employing a different type of aerosol and/or activation model (see Table 3). These simulations groups are roughly designed to exhibit some of the same variability shown in *Twohy et al.* [2005, Figure 4]. Also, the three groups utilizing the activation curve for a mixture of soluble and insoluble aerosol have been designed to fit within the extremes produced by the carbon activation model with the amount of ammonium sulfate mass fraction being $\epsilon_m = 0.02$, $\epsilon_m = 0.1$, and $\epsilon_m = 0.44$.

[28] Given the lognormal aerosol distribution an increasing amount of aerosol was added to the second mode, (see Table 2) $N_3 = 130, 260, 520,$ and 1040 cm^{-3}, for the 4 different simulations in each group. Each simulation name, except reference runs-REF, starts with an abbreviation of the aerosol type added to the second mode, e.g., AS-ammonium sulfate, PHO-hydrophobic BC, PHI-hydrophilic BC, MIX-internally mixed aerosol with different mass fraction (ϵ_m) of soluble aerosol, and ends with concentration of additional aerosol added. Hence, the only difference between the simulation groups is the type of aerosol that is added to the background distribution, and the only difference between the simulations within a group is the quantity of aerosol being added to the reference concentration.

Table 3. Overview of all Simulations[a]

Simulation	Group	Distribution Type	Cond. Model	ΔG	ϵ_m	Aerosol Type
REF	0	1	equation (13)			AS
REF_A1*	0	1	equation (13)			AS
REF_A2*	0	1	equation (13)			AS
AS_130	1	1 + 2	equation (13)			AS
AS_260	1	1 + 3	equation (13)			AS
AS_520	1	1 + 4	equation (13)			AS
AS_1040	1	1 + 5	equation (13)			AS
PHO_130	2	1 + 2	equation (14)	33.6		BC
PHO_260	2	1 + 3	equation (14)	33.6		BC
PHO_520	2	1 + 4	equation (14)	33.6		BC
PHO_1040	2	1 + 5	equation (14)	33.6		BC
PHI_130	3	1 + 2	equation (14)	−5.2		BC
PHI_260	3	1 + 3	equation (14)	−5.2		BC
PHI_520	3	1 + 4	equation (14)	−5.2		BC
PHI_1040	3	1 + 5	equation (14)	−5.2		BC
MIX_P1_130	4	1 + 2	equation (15)		0.02	AS and BC
MIX_P1_260	4	1 + 3	equation (15)		0.02	AS and BC
MIX_P1_520	4	1 + 4	equation (15)		0.02	AS and BC
MIX_P1_1040	4	1 + 5	equation (15)		0.02	AS and BC
MIX_P2_130	5	1 + 2	equation (15)		0.1	AS and BC
MIX_P2_260	5	1 + 3	equation (15)		0.1	AS and BC
MIX_P2_520	5	1 + 4	equation (15)		0.1	AS and BC
MIX_P2_1040	5	1 + 5	equation (15)		0.1	AS and BC
MIX_P3_130	6	1 + 2	equation (15)		0.44	AS and BC
MIX_P3_260	6	1 + 3	equation (15)		0.44	AS and BC
MIX_P3_520	6	1 + 4	equation (15)		0.44	AS and BC
MIX_P3_1040	6	1 + 5	equation (15)		0.44	AS and BC

[a]Condensation model refers to equation used to calculate equilibrium supersaturation, parameters ΔG [kJ/mol] and ϵ_m - constants used in corresponding equations, aerosol type: AS - ammonium sulfate, BC - black carbon, AS and BC - internally mixed ammonium sulfate and black carbon. Simulations marked with * use diffusivity of water vapor and thermal conductivity of air modified to take into account non-continuum effect.
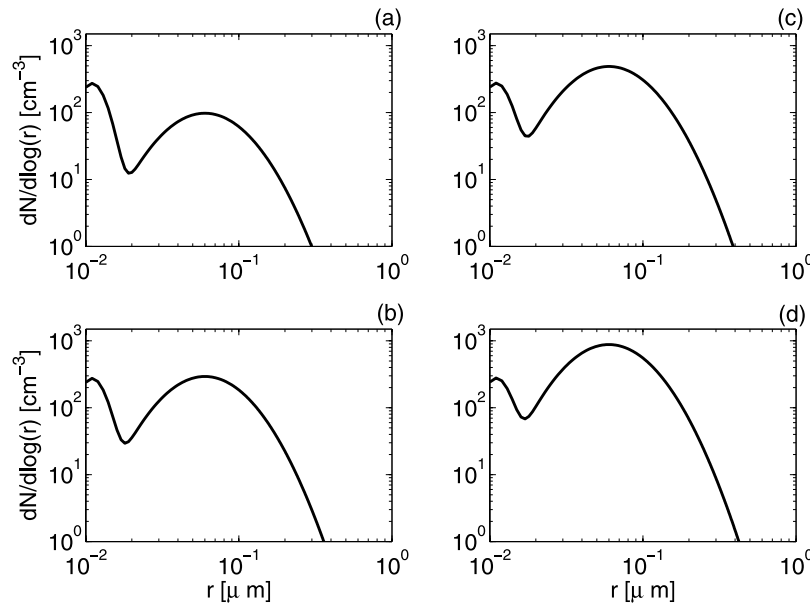
Figure 1. Initial aerosol size distributions for a given simulation group. (a) $N_3 = 0$ cm^{-3} (distribution type 1 or reference state when AS aerosol are specified), (b) $N_3 = 260$ cm^{-3} (distribution type 1 + 3), (c) $N_3 = 520$ cm^{-3} (distribution type 1 + 4), and (d) $N_3 = 1040$ cm^{-3} with N_3 (distribution type 1 + 5) representing the addition of aerosol to the accumulation mode, N_3, via equation (20), see 2. Note that $N_3 = 130$ cm^{-3} (distribution type 1 + 2) was not shown due to space considerations.

[29] Figure 1 provides a graphical illustration of the aerosol distributions for the reference run and 3 sensitivity runs, e.g., (Figure 1a) the reference run-REF (255 cm^{-3}), (Figure 1b) simulation with additional 260 aerosol cm^{-3}, (Figure 1c) simulation with additional 520 aerosol cm^{-3}, (Figure 1d) and simulation with additional 1040 aerosol cm^{-3}, within a group. Parameters used to calculate equilib-

rium supersaturation are given in Table 3. Note, all simulation groups share these common distributions with the only difference being the type of aerosol added to the second mode.

[30] The increasing number of aerosol in the last mode was roughly designed to bracket the peak in aerosol at $r = 0.055$ μm, as shown by *Twohy et al.* [2005, Figure 2], and
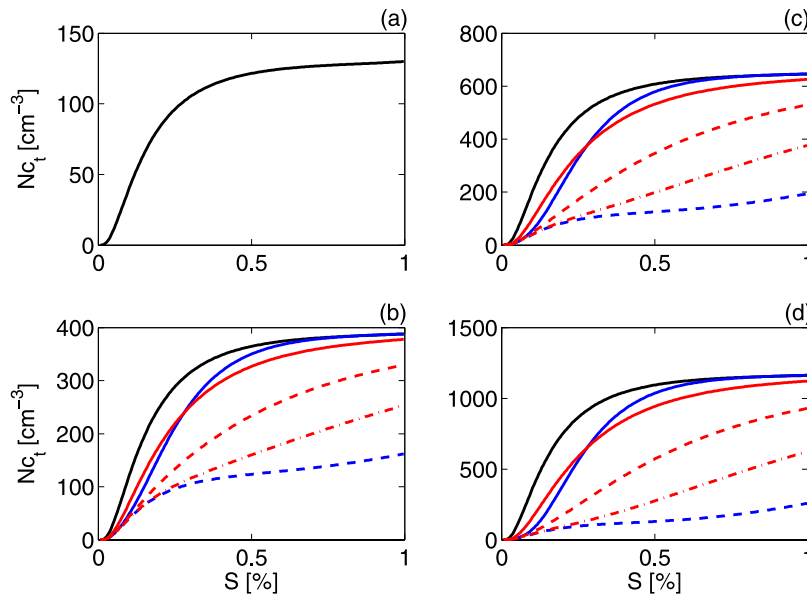
Figure 2. Number of activated cloud droplets (Nc_t) versus supersaturation produced in equation (13) for AS aerosol (solid black line), in equation (14) for BC aerosol (blue line, $\Delta G = -5.2$; dashed blue line, $\Delta G = 33.6$), and in equation (15) for an internal mixture of AS and BC aerosol ($\epsilon_m = 0.02$, solid red line; $\epsilon_m = 0.1$, dashed red line; $\epsilon_m = 0.44$, dashed-dotted red line) as a function of increasing number of these aerosol, (b) 260 cm^{-3}, (c) 520 cm^{-3}, and (d) 1040 cm^{-3}, being added to (a) the reference state through N_3.
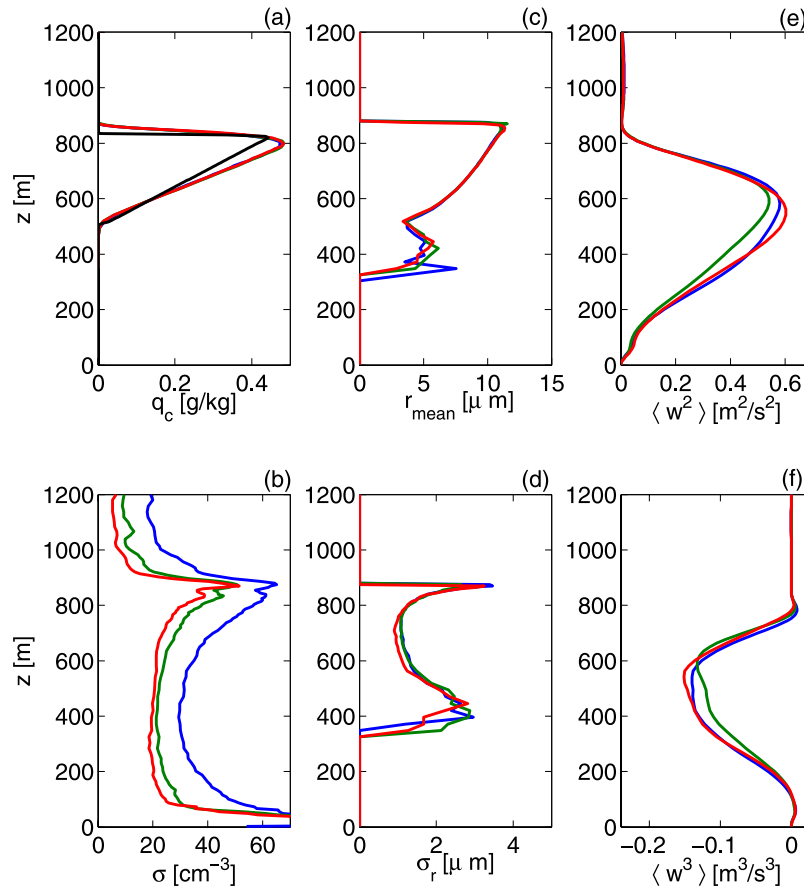
Figure 3. Graphs of mean vertical profiles of (a) cloud water mixing ratio (black line represents the observed cloud water mixing ratio field from RF01), (b) the standard deviation for the total number of particles, aerosol plus cloud droplets, (c) r_{mean}, (d) the standard deviation for r_{mean}, (e) variance of the vertical motion field, (f) third moment of the vertical motion field using 0.45 (blue line), 1.8 (green line), and 7.2 (red line) million particles for the aerosol distribution of the reference run.

hence, depending on aerosol type, should lead to significant differences in the aggregate curves of Nc_t versus aerosol concentration from each simulation group. As an illustration of these potential differences in the absence of dynamics, Figure 2 shows Nc_t as a function of critical supersaturation, diagnosed from equations (13)–(15). As evident from this figure, differences between the groups become more apparent with increasing supersaturation and aerosol number with groups 1 and 2 (Table 3) activating the most and least number of aerosol, respectively.

3.3. Validation

[31] The reference simulation described in the previous section was run for a time period of 4 hours. To help increase the computational efficiency of the numerous sensitivity simulations, they were initialized using data 80 minutes into the reference simulation at a time period when dynamical fields have become somewhat established, with these simulations running for another 160 minutes. When computing mean fields, such as the mean vertical profile of q_c, or other key mean statistics, model results have been averaged in space and time over the last 2 hours of a given simulation.

[32] Given that the LCM framework is somewhat new to atmospheric science and is subject to sampling errors,

considerable testing has been done to ensure its robustness with respect to other established methods, such as the bin approach. Though details of this testing will be deferred for a future paper, two additional simulations that are identical to the reference simulation, except that the total number of particles was either increased or decreased by a factor of four, were conducted to examine the impact of sampling errors. Note, by adjusting the total number of particles utilized in a given simulation, the initial aerosol concentration within a grid cell does not change, with only the multiplier used to determine the actual number of aerosol particles represented by each Lagrangian particle changing. For example, if 100 aerosol particles are actually present in a given volume, but only 10 Lagrangian particles are being used in a simulation to represent these 100 aerosol particles, then the multiplier is 10. However, when the number of particles in a simulation is increased or decreased, the multiplier needs to be adjusted to ensure that the actual concentration, 100 aerosol particles per volume, remains the same.

[33] Figure 3a shows q_c fields (q_c computed by knowing particle location within a grid cell) as a function of height from all three simulations are nearly independent of particle number with most other mean quantities such as Nc_t (not
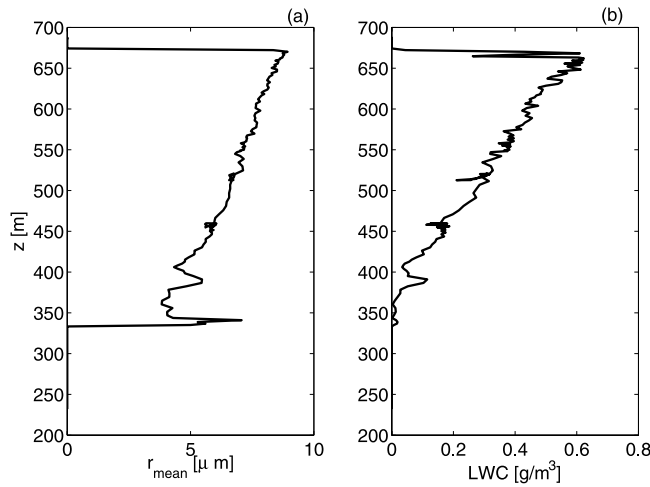
Figure 4. Vertical profiles of (a) r_{mean} and (b) liquid water content obtained during RF03 of DYCOMS-II.

shown), also being roughly independent of the total number of aerosol particles within the computation domain; however, r_{mean} (Figure 3c), σ_r (standard deviation of r_{mean}, Figure 3d) $\langle w^2 \rangle$ (variance of w, Figure 3e), and $\langle w^3 \rangle$ (third moment of w, Figure 3f) do contain some small variability, especially near cloud bottom. In contrast, departures in standard deviation for total particle number field, aerosol plus cloud droplets (see Figure 3b) are, as expected, larger than those observed for the other quantities.

[34] Three other important aspects are evident in Figure 3 with the first being the relatively good comparison between the mean q_c fields and the vertical motion statistics [see *Stevens et al.*, 2005, Figure 5] with the observed fields. Moreover, unlike most model results by *Stevens et al.*

[2005], the stratus cloud produced by LCM framework did not, in fact, go up during the 4 h simulation. Another interesting aspect shown in Figure 3c is the secondary maximum in r_{mean} at the cloud bottom with this maximum being also evident in data (see Figure 4) obtained from flight three (RF03) of DYCOMS-II (no data was available from RF01). Also, as the last item of interest, Figure 3b suggests that 1.8 million particles, in place of using 4 times as many, appears to be a sufficient number to minimize the impact of sampling errors.

[35] Because the condensational model contains some uncertainty, especially with regard to the noncontinuum effect, two sensitivity simulations were conducted in which the diffusivity of water vapor and thermal conductivity of air were modified as in *Nenes et al.* [2001]. For simulation *REF_A1* values of $a_c = 0.03$ for the condensation coefficient and $a_t = 0.96$ for the thermal accommodation coefficient were used, whereas for simulation *REF_A2* $a_c = 1.0$ with a_t being the same as used in *REF_A1*. Results of these simulations are summarized in Table 4 and show that the noncontinuum effect has a small influence on cloud properties. Nc_t/r_{mean} decreases/increases about 10%/5% with respect to the reference run with little differences in mean quantities between *REF_A1* and *REF_A2*. Hence given the small changes in mean quantities when the noncontinuum effect was active, and the uncertainty in a_c and a_t, for subsequent simulations the noncontinuum effect was not utilized within the condensational model.

4. Results

[36] In this section various results from the simulations produced by the LCM framework will be presented. Before presenting a detailed analysis of key cloud properties as a

Table 4. Key Cloud Quantities From all Simulations Produced by Averaging Results in Both Space and Time for the Last 2 h of the Simulations

| Simulation	r_{mean} [μm]	σ_r [μm]	$Nc_{BC/MIX}$ [cm^{-3}]	Nc_{AS} [cm^{-3}]	Nc_t [cm^{-3}]
REF	8.2	2.3	-	103.4	103.4
REF_A1	8.6	2.4	-	95.0	95.0
REF_A2	8.5	2.4	-	96.1	96.1
AS_130	6.7	1.8	-	181.1	181.1
AS_260	6.0	1.6	-	251.5	251.5
AS_520	5.3	1.4	-	344.6	344.6
AS_1040	4.6	1.3	-	427.2	427.2
PHO_130	8.2	2.3	3.6	103.5	105.6
PHO_260	8.2	2.3	5.3	102.9	106.3
PHO_520	8.0	2.2	11.3	103.4	111.4
PHO_1040	7.9	2.2	22.5	103.1	118.8
PHI_130	7.0	2.0	78.3	91.8	169.0
PHI_260	6.2	1.7	148.1	85.5	232.4
PHI_520	5.5	1.6	257.3	76.5	331.8
PHI_1040	4.6	1.4	456.8	64.4	516.5
MIX_P1_130	7.8	2.2	19.3	102.3	121.0
MIX_P1_260	7.6	2.1	32.1	99.8	131.1
MIX_P1_520	7.3	2.1	55.8	99.7	151.2
MIX_P1_1040	6.7	1.9	97.1	95.3	190.1
MIX_P2_130	7.4	2.1	41.7	98.3	139.3
MIX_P2_260	6.9	2.0	72.6	94.2	166.0
MIX_P2_520	6.2	1.7	144.4	94.5	237.8
MIX_P2_1040	5.6	1.6	232.6	88.1	318.7
MIX_P3_130	7.0	2.0	73.3	93.8	166.2
MIX_P3_260	6.3	1.8	135.4	89.8	224.3
MIX_P3_520	5.5	1.6	248.6	84.8	332.1
MIX_P3_1040	4.9	1.5	403.4	73.8	475.4
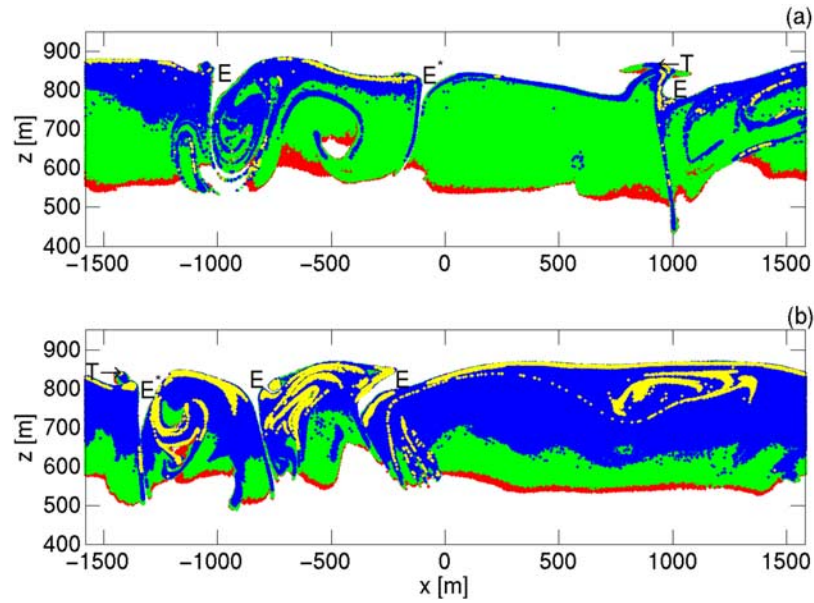
Figure 5. Spatial location of activated cloud droplets over a portion of the vertical domain from simulations (a) PHI_1040 and (b) PHI_260 at 4 h. The size of the droplets is indicated by the following colors: $r \leq 3$ μm (red), 3 μm $< r \leq 6$ μm (green), 6 μm $< r \leq 9$ μm (blue), and $r \geq 9$ μm (yellow). The locations marked by "E" denote regions, where entrainment events are taking place with * denoting the two areas blown up in Figure 7 and "T" showing the ending location of the trajectories shown in Figure 6.
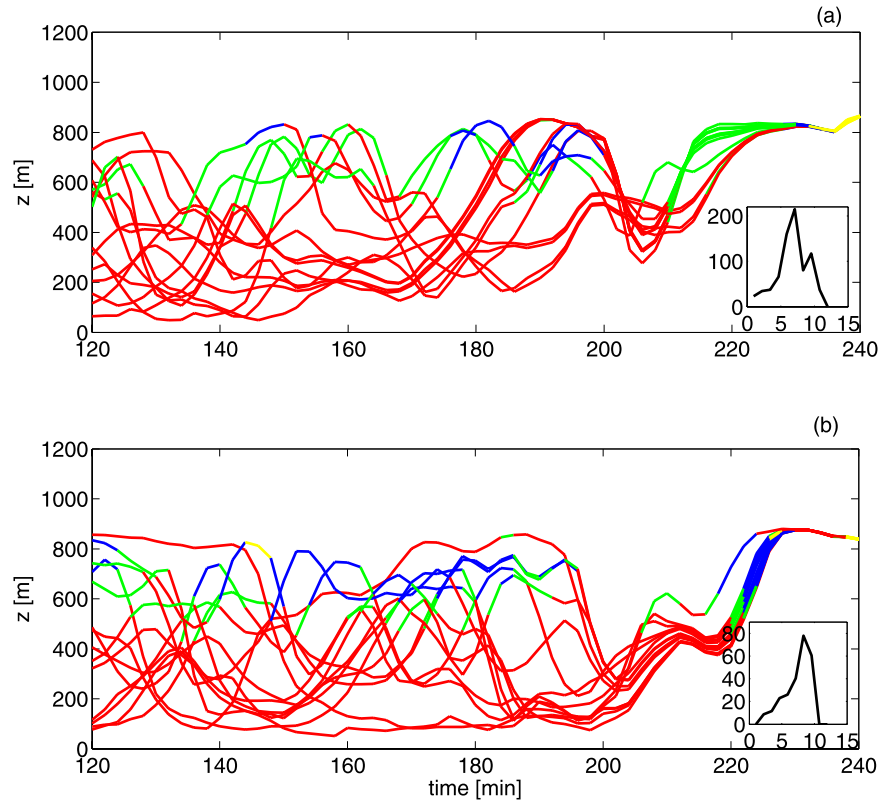
Figure 6. Trajectories of 14 particles from simulations (a) PHI_1040 and (b) PHI_260 with colors indicating droplet size (same color scheme as in Figure 5). The two inserts represent cloud droplet spectra taken from the two grid cells marked by T in Figure 5.
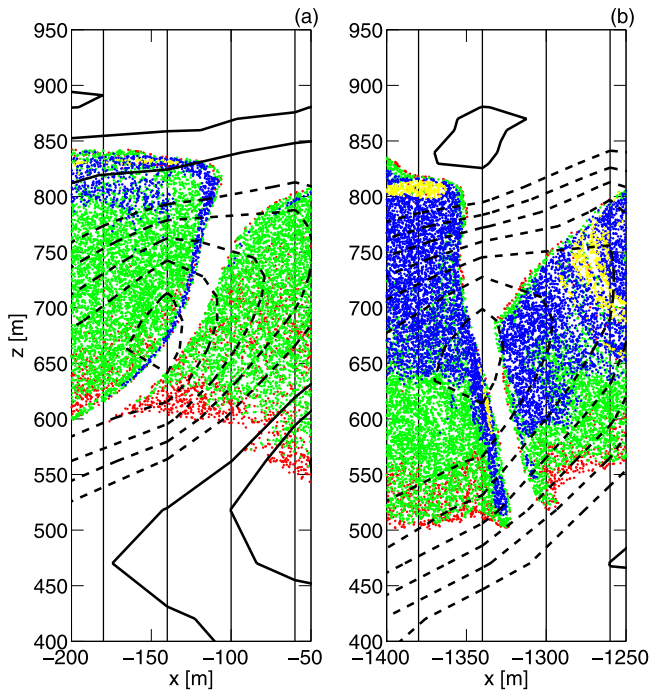
Figure 7. Enlargement of two entrainment events occurring within simulations (a) PHI_1040 and (b) PHI_260 (denoted by * in Figure 5) with colors indicating cloud droplet size as in the previous two figures and the thin vertical lines denoting the grid cell boundaries in the x direction. Thick black lines represent contours of vertical velocity with solid/dashed contours signaling areas of positive/negative vertical motions for a contour interval of 0.2 m s^{-1}.

function of aerosol type and number, a few representative results highlighting unique aspects of the model will be shown. For example, one of the distinctive aspects of a Lagrangian model is its ability to both show particle location and to track particles. Figure 5 reveals particle locations and sizes from two disparate simulations, PHI_260 and PHI_1040, with the figure clearly demonstrating the models ability to resolve fine-scale cloud features that would be difficult for an Eulerian model to produce at the same resolution. Variations in cloud droplet size, directly related to differences in aerosol number, can also be seen in the figure with significantly larger droplets being present in the simulation containing the lower aerosol concentrations.

[37] Figure 5 further reveals that small droplets are usually found near the cloud bottom with the radii of the droplets typically growing as the cloud top is approached. This structure is in general agreement with the classical view of an adiabatic cloud, where droplets are activated near the cloud bottom and continue growing in the updrafts. Figure 6, showing trajectories of 14 particles that ended up at nearly the same spatial location from either simulation PHI_260 or PHI_1040, serves to quantify this relationship between movement and the growth of droplets, with trajectories of select particles from both simulations showing that cloud droplets do grow rather rapidly during ascent within the stratus cloud. Likewise, the broad cloud droplet spectra

found within the grid cells marked "T" in Figure 5 from the two simulations are the result of particles coming from various places within the computational domain, and thus, per previous discussions in the introduction, would be very difficult to reproduce with a parcel model.

[38] Another feature apparent in both simulations is the multiple occurrence of entrainment events, denoted by "E" in Figure 5, with these events indicative of strong downward motions that result in the rapid evaporation of smaller cloud droplets leaving relatively fast falling large droplets in narrow subgrid cloud filaments. To better illustrate the spatial extent of these filaments, Figure 7 shows enlargements near two select entrainment events (denoted by E* in Figure 5) from simulation PHI_1040 and PHI_260 with Figure 7 clearly illustrating that the filaments are much smaller than the horizontal grid spacing of 40 m and are present near regions of downward motions. Also, Figure 7 is consistent with the speculation of *Lu and Seinfeld* [2007] that the peak of σ_r near cloud bottom is the result of "entity" mixing. However, in contrast to a hypothesis put forth by *Lu and Seinfeld* [2007], Figure 7 suggests that the source of bigger droplets is not horizontal mixing, but rather downward motions that advect big droplets from cloud top to bottom. Furthermore, because the observed third moment of the vertical motion field [see *Stevens et al.*, 2005, Figure 5] is negative, this observation also suggests the occurrence of regions of downward motions that could advect large droplets within entrainment events.

4.1. Aerosol Impact on Key Cloud Quantities

[39] As discussed in the introduction, a key aspect of this paper is to demonstrate the impact of a polluted air mass, composed of insoluble carbon aerosol of varying "wetness", on a stratus field. In particular, results in this section will highlight two limiting regimes, either all carbon aerosol are fresh (hydrophobic, simulation group 2) or are relatively old (hydrophilic, simulation group 3) with cloud droplets growing on this aerosol via the BC activation curve, equation (14). Note, the only difference implied in these simulations is that the type and/or age of carbon particles is changing with both the distribution and number of these aerosol remaining fixed. However, in all actuality, carbon aerosol in the atmosphere are almost always attached or internally mixed with some type of soluble particle, such as ammonium sulfate. In fact, in a subsequent section results from a few simulations employing mixed aerosol, along with the appropriate activation model, will be shown to help establish the link between the limiting regimes presented in this section and what may be present in the atmosphere.

[40] Contours of q_c from simulations employing an aerosol spectra partially composed of either hydrophobic (simulation group 2) or hydrophilic (simulation group 3) carbon particles of varying number, N_3, (see Table 2) are shown in Figure 8 with the q_c fields appearing to be independent of both aerosol number and type. Figure 9 showing mean vertical profiles of q_c from the same two simulation groups provides further evidence for this dependence with only small differences in the mean q_c fields from the six simulations comprising the two groups. However, unlike q_c, vertical profiles of mean Nc_t (see Figure 10) do appear to depend on aerosol number and type with large differences between the two simulation groups now being evident.
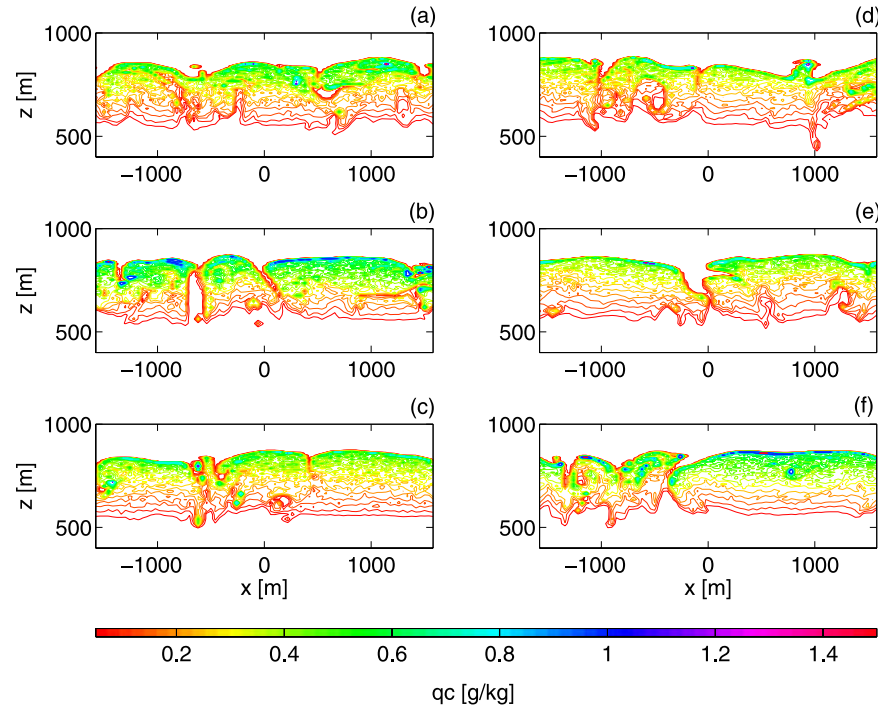
Figure 8. Contours of q_c at hour 4 over the entire computational domain for the following simulations: (a) PHO_1040, (b) PHO_520, (c) PHO_260, (d) PHI_1040, (e) PHI_520, and (f) PHI_260 with the scale in units of g kg^{-1}.

[41] Hence these results suggest that not only should q_c be independent of aerosol number and type, but the primary driver of q_c, vertical motions, should also be independent of aerosol properties. For example, Figure 11 reveals only a small dependence of the mean vertical profiles of vertical velocity statistics with regard to aerosol type (hydrophobic BC aerosol—simulation group 2 versus hydrophilic BC aerosol—simulation group 3), but little dependence with regard to number. Note, because the magnitude of downward motions is related to the evaporation of mainly the small droplets and that the simulations employing hydro-
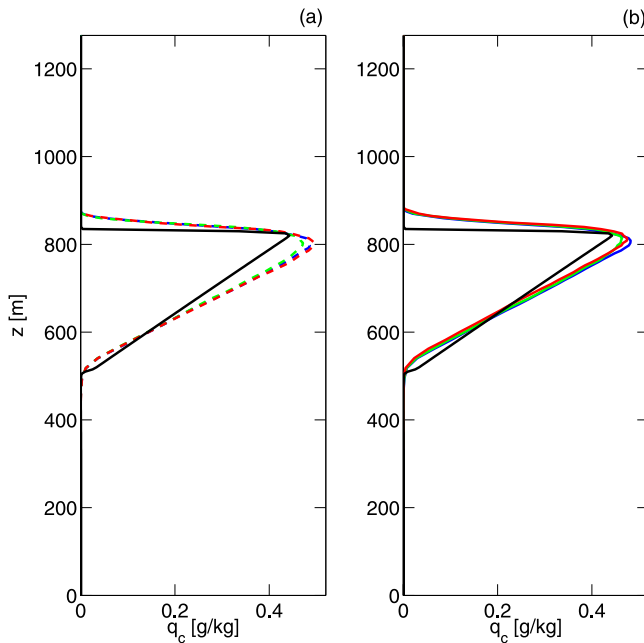
Figure 9. Vertical profiles of mean q_c from simulation group (a) 2 (PHO_260, dashed blue line; PHO_520, dashed green line; PHO_1040, dashed red line) and (b) 3 (PHI_260, blue line; PHI_520, green line; PHI_1040, red line) with the black line denoting the observed q_c field from RF01.
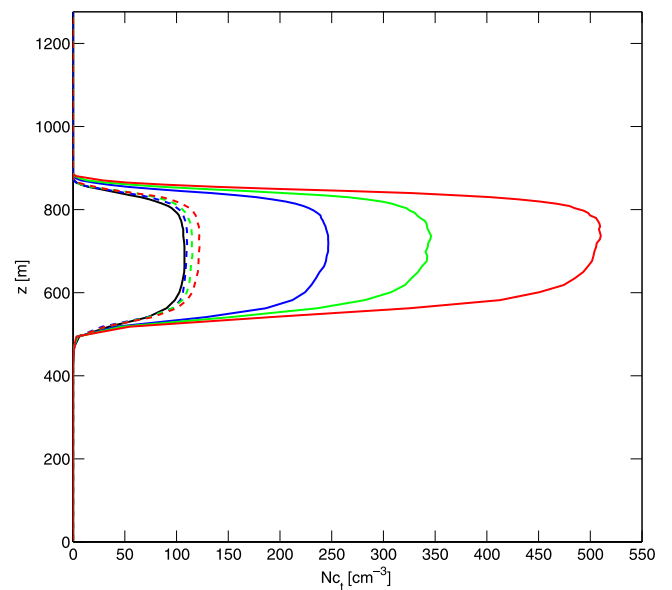
Figure 10. Vertical profiles of mean Nc_t with the reference solution (solid black line) used in place of the observed Nc_t with line colors, as in the previous figure.
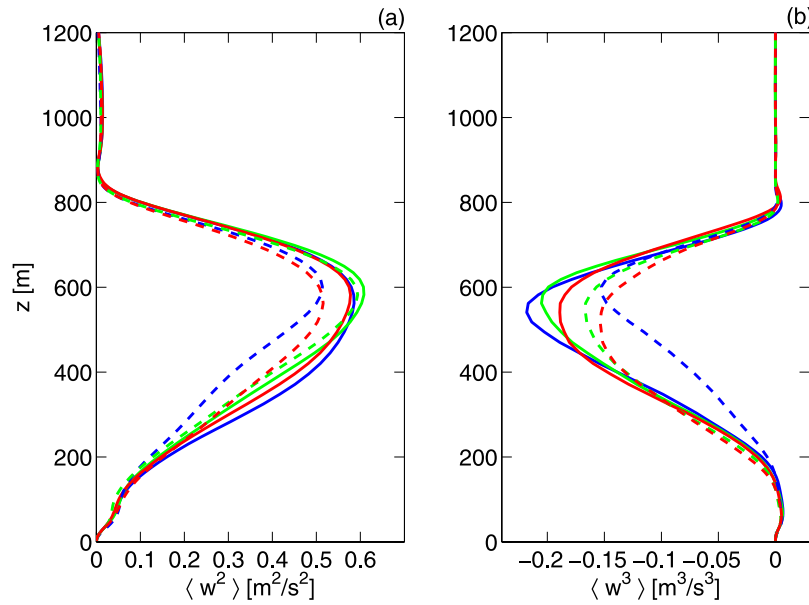
Figure 11. Vertical profiles of (a) the variance and (b) the third moment of w for the following simulations: PHI_260 (blue line), PHI_520 (red line), PHI_1040 (green line), PHO_260 (blue dashed line), PHO_520 (red dashed line), and PHO_1040 (green dashed line).

philic aerosol produced considerably more cloud droplets than the hydrophobic simulations, downward motions should be, not unexpectedly, larger in these simulations. In fact, given the rather large differences in cloud droplet number, it is somewhat surprising that the differences are, in fact, not bigger.

[42] The typical inverse correlation between increasing Nc_t and decreasing r_{mean} in the hydrophilic simulation group—in agreement with what was observed in the MAST

ship track program [*Ferek et al.*, 2000] or in stratus clouds [*Yum and Hudson*, 2002]—is visible in Figure 12, except near the cloud bottom where the effect of entrainment from large particles moving rapidly downward and then being possibly captured in updrafts in neighboring clouds, appears to be a dominating factor in determining droplet size. In contrast, Figure 12 shows that for the hydrophobic simulation group, little change occurs in r_{mean} for an increasing number of "nonwetting" aerosol, but significant differences
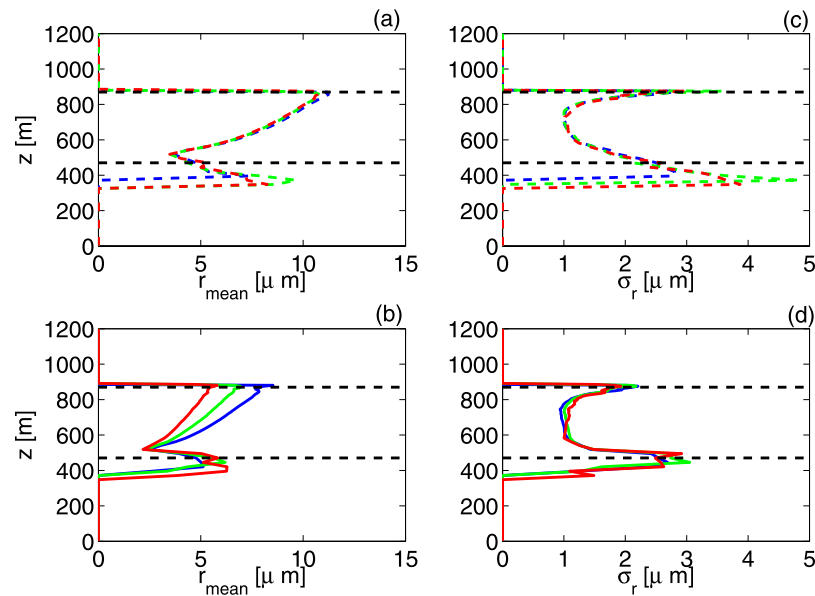

Figure 12. Vertical profiles of (a) r_{mean} for simulation group 2, (b) r_{mean} for simulation group 3, (c) standard deviation of r_{mean} for simulation group 2, and (d) standard deviation of r_{mean} for simulation group 3 with the line colors the same as in the previous two figures. The dashed black lines indicate the average location of either the cloud top or bottom based upon the analysis of the q_c fields.
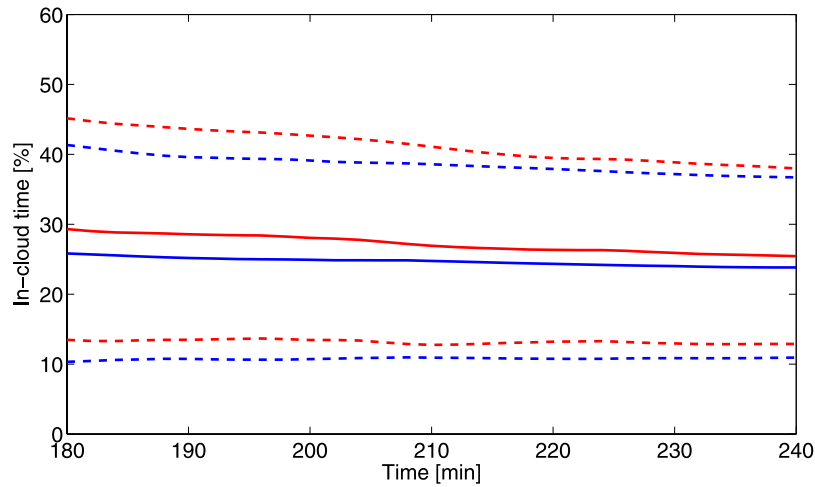
Figure 13. Mean in-cloud time (solid lines) and standard deviation (dashed lines) from simulations PHI_260 (blue line) and PHI_1040 (red line) with statistics normalized by integration time.

between the simulations are still evident at the cloud bottom due to entrainment. For example, at the points marked E in Figure 5 large droplets can be seen extending from the top of the cloud to the bottom, with these regions being associated with relatively strong downward motions and a corresponding short time scale that prevents the evaporation of the larger cloud droplets. Thus the occasional presence of these large droplets near or below the average location of the cloud bottom is responsible for the secondary maximum in r_{mean} shown in Figure 12 and is in agreement with observations from RF03 of DYCOMS-II (see Figure 4).

4.2. Aerosol Recycling

[43] Results from observations and numerical models suggest that the time droplets spend in a cloud or the in-cloud time, τ_r, can affect drizzle formation, cloud chemistry, and the spectra of cloud droplets and aerosol [*Feingold et al.*, 1996; *Feingold et al.*, 1998; *Kogan*, 2006; *Seinfeld and Pandis*, 1998] and hence gathering in-cloud time statistics from the LCM framework is an important diagnostic quantity. Further, since a large number of particles must be used during a given simulation to ensure proper sampling, the current predictive modeling approach employs at least an order magnitude more particles than previous diagnostic modeling approaches, e.g., *Kogan* [2006], that attempted to quantify τ_r. To quantify τ_r, particles were tracked during the last 2 hours of a simulation, with the in-cloud time being the total time spent at locations for which the supersaturation was greater or equal to zero.

[44] Figures 13–14 reveal τ_r statistics from two simulations, PHI_260 and PHI_1040, with these figures indicating only a weak dependence of τ_r with respect to aerosol number. The figures show that on average a particle spends approximately twenty five percent of its time in a cloud, with this in cloud percentage being larger than that produced by *Kogan* [2006] (sixteen percent, per Table 2) in his diagnostic analysis. Additionally, eddy turnover time, $\tau_s = L/\sigma_w$, for the current simulation is approximately 18 min which is smaller than the 25 min. time period a particle typically exists within the cloud, suggesting that, as also indicted in Figure 6, particle trajectories within a cloud can

consist of multiple up and down cycles with particles eventually exiting the cloud during strong entrainment events.

[45] Given that an aerosol particle may spend approximately twenty five percent of a given time period within a marine stratocumulus cloud, significant changes in chemical composition of an aerosol particle may occur, i.e., upon collision with another cloud droplet containing an entirely different aerosol particle. Specifically, a hydrophobic carbon aerosol particle during recycling could acquire, via collision, significant amounts of ammonium sulfate to the extent that the resulting aerosol mixture is now hydrophilic. Hence downstream of a carbon source within an environment containing numerous stratus clouds, aerosol particles could undergo significant modification in their
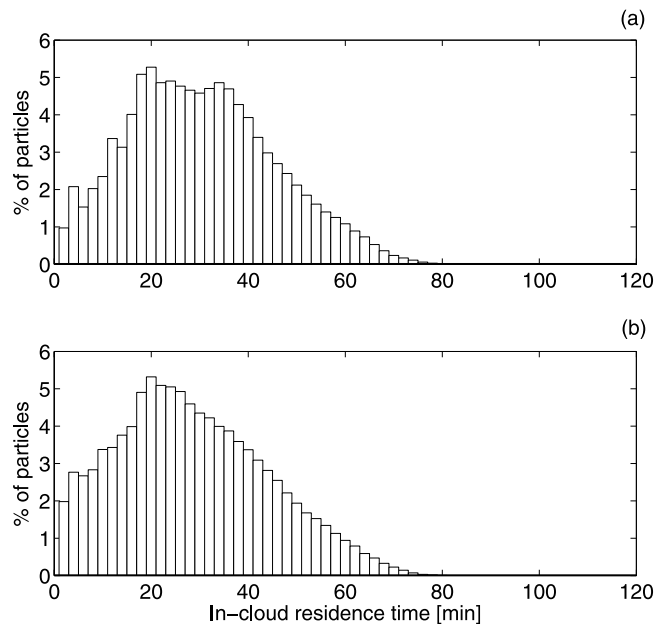

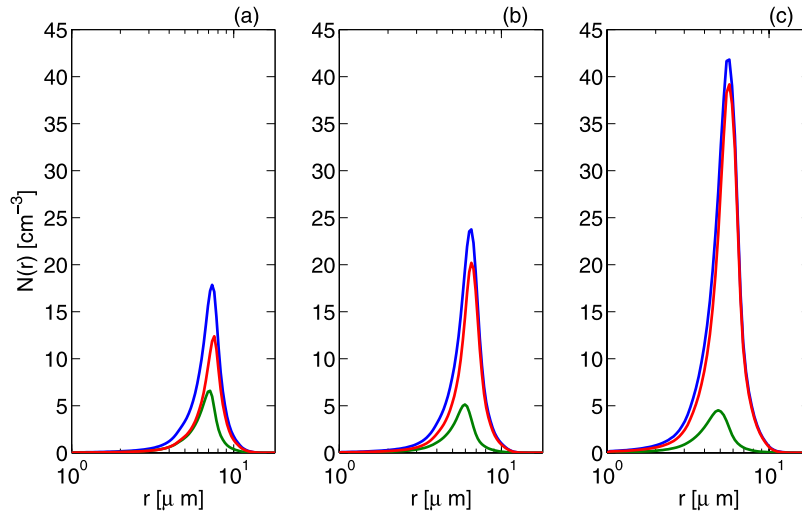**Figure 14.** Histogram of in-cloud residence time from simulations (a) PHI_1040 and (b) PHI_260.

Figure 15. Cloud droplet spectra averaged over space and time for the following simulations: (a) PHI_230, (b) PHI_520, and (c) PHI_1040 with the red line the spectrum on BC aerosol, the green line the spectrum on ammonium sulfate and the blue line the spectrum resulting from summing the two aerosol.

chemical makeup, thus inducing significant changes in cloud properties.

4.3. Overview and Potential Impact on Bulk Models

[46] Table 4 summarizes results from all simulations. It shows r_{mean}, σ_r, and cloud droplet number concentrations on AS aerosol (Nc_{AS}), on black carbon aerosol (Nc_{BC}), and Nc_t averaged over the entire domain for the last two hours and for all simulations. Note for simulation groups 4–6, where the additional aerosol is composed of an internal mixture of BC and AS, Nc_{MIX} on this aerosol is reported in the same column as Nc_{BC}. This table clearly illustrates the increasing disparity in mean radius between hydrophilic and hydrophobic BC aerosol simulations with increasing aerosol number. Mean droplet spectra from the simulations employing the BC activation model are shown in Figures 15–16 and serve to supplement the data shown in Table 4, while also illustrating that the spectra are relatively Gaussian in

shape. Table 4 also quantifies results from the simulation groups employing the other activation models and shows that for simulations employing increasing quantities of ammonium sulfate (group 1), a hydrophilic aerosol, key cloud quantities are roughly similar to those produced by the hydrophilic BC simulations. Likewise, for the simulations employing a mixture of ammonium sulfate and BC (groups 4, 5 and 6), primary cloud quantities lie between the two extremes of the BC simulations with increasing amounts of ammonium sulfate within the mixture producing results that trend toward the hydrophilic BC simulations.

[47] As discussed in the previous section, BC aerosol could combine with other aerosol, such as ammonium sulfate, during the recycling process leading to aerosols represented by simulation groups 4–6. Thus, given that these type of aerosol particles should represent a majority of particles within a real atmosphere, simulation groups 4–6 are probably not that far removed from what occurs within marine
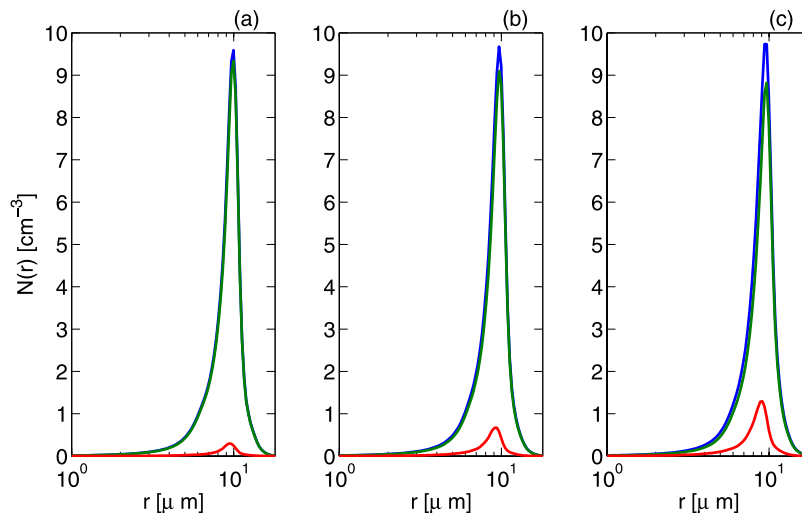

Figure 16. Same as in Figure 15, except for the hydrophobic BC simulations.
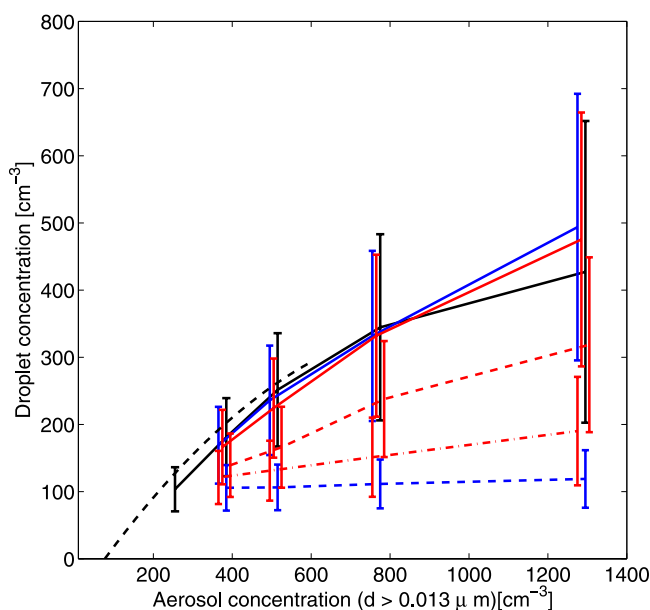
Figure 17. Cloud droplet number concentration as a function of aerosol concentration with black dashed line from DYCOMS-II [*Twohy et al.*, 2005], black solid line from simulation group 1 (AS_130, AS_260, AS_520, AS_1040), blue line from simulation group 2 (PHO_130, PHO_260, PHO_520, PHO_1040), blue dashed line from simulation group 3 (AS_130, AS_260, AS_520, AS_1040), red solid line from simulation group 4 (MIX_P1_130, MIX_P1_260, MIX_P1_520, MIX_P1_1040), red dashed line from simulation group 5 (MIX_P2_130, MIX_P2_260, MIX_P2_520, MIX_P2_1040), and red dot-dashed line from simulation group 6 (MIX_P3_130, MIX_P3_260, MIX_P3_520, MIX_P3_1040).

stratus clouds either near carbon sources (simulation group 4) or far downstream from the sources (simulation group 6). Further, since in a realistic setting the ratio of ammonium sulfate (or any other hydrophilic aerosol) to carbon is obviously not constant in time or space, future simulations are needed to understand the impact of various distributions of these mixed aerosol particles on marine stratus.

[48] A key relationship that is of potential use in bulk microphysical models is the association between aerosol number concentration and Nc_t. Figure 17 shows this relationship from the various simulation groups with observational results being relatively close to simulation groups that utilized primarily hydrophilic aerosol (simulation groups 1, 3, and 6). However, it should be noted for all simulations both the initial and boundary conditions were for RF01. Hence, to accurately reproduce the dashed line shown in Figure 17, both the initial and boundary conditions should be modified to represent actual conditions observed from the various flights that went into producing the dashed line. Additionally, for the various curves shown in *Twohy et al.* [2005, Figure 4], obtained from various other field programs, the LCM framework could be used in future simulations of these field programs to determine whether or not the suppression of cloud droplet number concentrations obtained from more "polluted" environments was actually due to the aerosol makeup or simply a reduction in the

supersaturation field. Obviously, if future simulations suggest aerosol type was the cause of the nearly flat lines shown in *Twohy et al.* [2005, Figure 4], then, given a certain percentage increase in aerosol number, changes in shortwave radiation impacts will be much smaller in a primarily hydrophobic aerosol environment.

5. Concluding Remarks and Future Directions

[49] A Lagrangian cloud model capable of efficiently simulating the condensational growth of cloud droplets from aerosol of various sizes and types was presented in this paper. Even with relatively coarse spatial resolution in the gas phase, the model was shown to be able to reasonably reproduce key cloud features observed during RF01, including the secondary maximum in droplet radii found at the bottom of the stratus cloud deck. Results from simulations presented in this paper clearly suggest that aerosol type matters under certain circumstances, e.g., within a marine stratus field downwind of a urban area, with results from this modeling study being supported by the observational work of *Hudson and Li* [1995]. Likewise, as was discussed in *Hudson* [2007], the previous findings of *Dusek et al.* [2006] whom demonstrated that number is of more importance than type for well-mixed continental air masses over Germany, may not be generally applicable downwind of continents producing large amounts of carbon-based aerosol particles, e.g., India. However, as previously discussed in the section describing the formulation of the initial aerosol distributions for the various sensitivity simulations, aerosol size can be as important as type for determining various cloud properties. Hence if the majority of aerosol produced over India or Germany are either very large or small in size, then the actual composition matters little with regard to the impact on cloud properties.

[50] The simulations shown in this paper serve as an initial first step toward determining the utility of using the LCM framework for modeling key cloud properties. Further, even though the current approach is less expensive than a two-dimensional bin model representing both cloud and aerosol droplet spectra, it still requires considerable computational resources and would be impractical to run in an operational setting. However, results from the model could be used to refine and develop parameterizations employed within much faster running bulk cloud models. Additionally, with the inclusion of collision-coalescence and chemistry, three-dimensional simulations employing the LCM framework could be used to answer fundamental questions regarding cloud-chemistry interactions as well as helping to supplement observational data from ship track studies or fields programs such as DYCOMS-II.

References

Ackerman, A., et al. (2000), Effects of aerosols on cloud albedo: Evaluation of Twomey's parameterization of cloud susceptibility using measurements of ship tracks, *J. Atmos. Sci.*, *57*, 2684–2695.

Albrecht, B. (1989), Aerosols, cloud microphysics and fractional cloudiness, *Science*, *245*, 1227–1230.

Barahona, D., and A. Nenes (2007), Parameterization of cloud droplet formation in large-scale models: Including effects of entrainment, *J. Geophys. Res.*, *112*, D16206, doi:10.1029/2007JD008473.

Bergstrom, R., P. Russell, and P. Hignett (2002), Wavelength dependence of the absorption of black carbon particles: Predictions and results from the TARFOX experiment and implications for the aerosol single scattering albedo, *J. Atmos. Sci.*, *59*, 567–577.

Clark, T. (1973), Numerical modeling of the dynamics and microphysics of warm cumulus convection, *J. Atmos. Sci.*, *30*, 857–878.

Crowe, C., M. Sommerfeld, and Y. Tsuji (1998), *Multiphase Flows With Droplets and Particles*, CRC Press, Boca Raton, Fla.

DaSilva, A., C. Sinfort, D. Pierrat, and S. Huberson (2006), A Lagrangian model for spray behaviour within vine canopies, *J. Aerosol Sci.*, *37*, 658–674.

Durkee, P., et al. (2000), The impact of ship-produced aerosols on the microstructure and albedo of warm marine stratocumulus clouds: A test of mast hypotheses 1i and 1ii, *J. Atmos. Sci.*, *57*, 2554–2569.

Dusek, U., et al. (2006), Size matters more than chemistry for cloud-nucleating ability of aerosol particles, *Science*, *312*, 1375–1378.

Feingold, G., B. Stevens, W. Cotton, and A. Frisch (1996), The relationship between in-cloud residence time and drizzle production in numerically simulated stratocummulus clouds, *J. Atmos. Sci.*, *53*, 1108–1122.

Feingold, G., S. Kreidenweis, and Y. Zhang (1998), Stratocummulus processing of gases and cloud condensation nuclei 1. Trajectory ensemble model, *J. Geophys. Res.*, *103*, 19,527–19,542.

Ferek, R., et al. (2000), Drizzle suppression in ship tracks, *J. Atmos. Sci.*, *57*, 2707–2728.

Flossmann, A. (1998), Interaction of aerosol particles and clouds, *J. Atmos. Sci.*, *55*, 879–887.

Fountoukis, C., and A. Nenes (2005), Continued development of a cloud droplet formation parameterization for global climate models, *J. Geophys. Res.*, *110*, D11212, doi:10.1029/2004JD005591.

Grabowski, W., and P. Smolarkiewicz (1990), Monotone finite-difference approximations to the advection-condensation problem, *Mon. Weather Rev.*, *118*, 2082–2097.

Gu, Z., Y. Zhao, Y. Li, Y. Yu, and X. Feng (2006), Numerical simulation of dust lifting with dust devils—Simulation of an intense vortex, *J. Atmos. Sci.*, *63*, 2630–2641.

Henson, B., and J. Robinson (2004), Dependence of quasi-liquid thickness on the liquid activity: A bulk thermodynamic theory of the interface, *Physical Rev. Letters*, *92*, 246,107–246,104.

Henson, B. F. (2007), An absorption model of insoluble particle activation: Application to black carbon, *J. Geophys. Res.*, *112*, D24S16, doi:10.1029/2007JD008549.

Hudson, J. (2007), Variability of the relationship between particle size and cloud-nucleating ability, *Geophys. Res. Lett.*, *34*, L08801, doi:10.1029/2006GL028850.

Hudson, J., and H. Li (1995), Microphysical contrasts in Atlantic stratus, *J. Atmos. Sci.*, *52*, 3031–3040.

Hudson, J., T. Garrett, P. Hobbs, and S. Strader (2000), Cloud condensation nuclei and ship track clouds, *J. Atmos. Sci.*, *57*, 2696–2706.

Iacono, G., and A. Reynolds (2005), A Lagrangian stochastic model for the dispersion and deposition of Brownian particles in the presence of a temperature gradient, *J. Aerosol Sci.*, *36*, 1238–1250.

Jeffery, C., and J. Reisner (2006), A study of cloud mixing and evolution using pdf methods. Part I: Cloud front propagation and evaporation, *J. Atmos. Sci.*, *63*, 2848–2864.

Kao, C.-Y., Y.-H. Hang, J. Reisner, and W. Smith (2000), Test of the volume-of-fluid method on simulations of marine boundary layer clouds, *Mon. Weather Rev.*, *128*, 1960–1970.

Kogan, Y. L. (1991), The simulation of a convective cloud in a 3D model with explicit microphysics. Part I: Model description and sensitivity experiments, *J. Atmos. Sci.*, *48*, 1160–1189.

Kogan, Y. (2006), Large-eddy simulation of air parcels in stratocumulus clouds: Time scales and spatial variability, *J. Atmos. Sci.*, *63*, 952–967.

Lu, M., and H. Seinfeld (2007), Effect of aerosol number concentration on cloud droplet dispersion: A large-eddy simulation study and implications for aerosol indirect forcing, *J. Geophys. Res.*, *111*, D02207, doi:10.1029/2005JD006419.

Margolin, L., J. Reisner, and P. Smolarkiewicz (1997), Application of the volume-of-fluid method to the advection-condensation problem, *Mon. Weather Rev.*, *125*, 2265–2273.

Martins, J., P. Artaxo, C. Liousse, J. Reid, P. Hobbs, and Y. Kaufman (1998), Effects of black carbon content, particle size, and mixing on light absorption from biomass burning in Brazil, *J. Geophys. Res.*, *103*, 32,041–32,050.

Matida, E., W. Finlay, C. Lange, and B. Grgic (2004), Improved numerical simulation of aerosol deposition in an idealized mouth-throat, *J. Aerosol Sci.*, *35*, 1–19.

Mellor, G., and T. Yamada (1974), A hierarchy of turbulence closure models for planetary boundary layers, *J. Atmos. Sci.*, *31*, 1791–1806.

Nenes, A., and J. H. Seinfeld (2003), Parameterization of cloud droplet formation in global climate models, *J. Geophys. Res.*, *108*(D14), 4415, doi:10.1029/2002JD002911.

Nenes, A., et al. (2001), Kinetic limitations on cloud droplet formation and impact on cloud albedo, *Tellus*, *53B*, 133–149.

Press, W., S. Teukolsky, W. T. Vetterling, and B. P. Flannery (1992), *Numerical Recipes in Fortran 77: The Art of Scientific Computing*, Cambridge Univ. Press, New York.

Pruppacher, H., and J. Klett (1978), *Microphysics of Clouds and Precipitation*, Springer, New York.

Reisner, J., A. Wyszogrodzki, V. Mousseau, and D. Knoll (2003), An efficient physics-based preconditioner for the, fully implicit solution of small-scale thermally driven atmospheric flows, *J. Comput. Phys.*, *189*, 30–44.

Reisner, J., V. Mousseau, A. Wyszogrodzki, and D. Knoll (2005), A fully implicit hurricane model with physics-based preconditioning, *Mon. Weather Rev.*, *133*, 1003–1022.

Rudzinski, W., and D. Everett (1992), *Absorption of Gases on Heterogeneous Surfaces*, Elsevier, New York.

Schwere, S., A. Stohl, and M. Rotach (2002), Practical considerations to speed up Lagrangian stochastic particle models, *Comput. Geosci.*, *28*, 143–154.

Seinfeld, J., and S. Pandis (1998), *Atmospheric Chemistry and Physics*, John Wiley, Hoboken, N. J.

Stevens, B., G. Feingold, W. R. Cotton, and R. L. Walko (1996a), Elements of the microphysical structure of numerically simulated nonprecipitating stratocumulus, *J. Atmos. Sci.*, *53*, 980–1006.

Stevens, B., R. Walko, G. Feingold, and W. Cotton (1996b), The spurious production of cloud edge supersaturations by Eulerian models, *Mon. Weather Rev.*, *124*, 1034–1041.

Stevens, B., et al. (2005), Evaluation of large-eddy simulations via observations of nocturnal marine stratocumulus, *Mon. Weather Rev.*, *133*, 1443–1462.

Twohy, C., et al. (2005), Evaluation of the aerosol indirect effect in marine stratocumulus clouds: Droplet number, size, liquid water path, and radiative impact, *J. Geophys. Res.*, *110*, D08203, doi:10.1029/2004JD005116.

Twomey, S. (1974), Pollution and planetary albedo, *Atmos. Environ.*, *8*, 1251–1256.

Yum, S., and J. Hudson (2002), Maritime/continental microphysical contrasts in stratus, *Tellus*, *54B*, 61–73.

_____

M. Andrejczuk, M. K. Dubey, B. Henson, C. A. Jeffery, and J. M. Reisner, Los Alamos National Laboratory, M.S. D401, Los Alamos, NM 87545, USA. (miroslaw@lanl.gov)